Blind Source Separation for Myelin Water Fraction Mapping Using Multi-Echo Gradient Echo Imaging

Jae Eun Song, Jaewook Shin, Hongpyo Lee, Ho Joon Lee, Won-Jin Moon, and Dong-Hyun Kim, *Member, IEEE*

***Abstract*— In conventional gradient-echo myelin water imaging (GRE-MWI), myelin water fraction (MWF) is estimated by fitting the multi-echo gradient recalled echo (mGRE) signal to a pre-assumed numerical model (e.g., multi-component exponential curves or three component exponential curves). However, in mGRE, imaging artifacts (e.g., voxel spread function and physiological noise) and noise render the signal to deviate from the numerical model, leading to misfit of the model parameters. Here, as an alternative to the model-based GRE-MWI, a blind source separation (BSS) technique for the separation of multi-exponential mGRE signal is proposed. Among the various BSS techniques, a modified robust principal component analysis (rPCA) is presented to separate signal sources by enforcing the data-driven properties such as "low rankness" and "sparsity." Considering the signal evolution of T_2^* relaxation (i.e., non-negative exponential decay), low rankness of exponential decay was enforced by nonnegative matrix factorization (NMF) and hankelization. This method provides the separation of slow-decaying, fast-decaying exponential components and artifact components from mGRE images. After the separation, MWF map is reconstructed as the ratio of the fast-decaying component to the total decaying components. The proposed method was demonstrated in numerical simulations and in vivo scans. The method provided a robust estimation of MWF in the presence of statistical noise and imaging artifacts.**

***Index Terms*— Magnetic resonance imaging, GRE-MWI, blind source separation, myelin water fraction, robust principal component analysis.**

Manuscript received November 14, 2019; revised January 9, 2020; accepted January 12, 2020. Date of publication January 20, 2020; date of current version June 1, 2020. This work was supported by the National Research Foundation of Korea (NRF) grant funded by the Korea government (MSIT) under Grant NRF-2019R1A2C1090635. *(Jae Eun Song and Jaewook Shin contributed equally to this work.) (Corresponding author: Dong-Hyun Kim.)*

Jae Eun Song, Jaewook Shin, Hongpyo Lee, and Dong-Hyun Kim are with the Department of Electrical and Electronic Engineering, Yonsei University, Seoul 03722, South Korea (e-mail: jaeeun1992@yonsei.ac.kr; shinjw0929@naver.com; oracle1127@naver.com; donghyunkim@yonsei.ac.kr).

Ho Joon Lee is with the Department of Radiology, Inje University College of Medicine, Haeundae Paik Hospital, Busan 48108, South Korea (e-mail: hojoon.lee@paik.ac.kr).

Won-Jin Moon is with the Konkuk University Medical Center, Department of Radiology, Konkuk University School of Medicine, Seoul 05030, South Korea (e-mail: mdmoonwj@gmail.com).

This article has supplementary downloadable material available at http://ieeexplore.ieee.org, provided by the authors.

Color versions of one or more of the figures in this article are available online at http://ieeexplore.ieee.org.

Digital Object Identifier 10.1109/TMI.2020.2967068

I. Introduction

IN CONVENTIONAL myelin water imaging (MWI), spin-echo (SE) images (referred here as 'SE-MWI') are acquired at multiple echoes to measure signal decay due to T_2 relaxation [1]. In white matter of the brain, it has been demonstrated that this signal has multiple T_2 components e.g., myelin water and axonal/extracellular water. In order to separate these multiple signal sources, the measured signal is fitted to numerical models representing multi-exponential T_2 relaxation [1], [2]. This allows the separation of fast-decaying myelin water signal (i.e., short T_2 component) and slow-decaying axonal/extracellular water signal (i.e., long T_2 component). Myelin water fraction (MWF) is then estimated as the ratio of the fast-decaying water signal to the total water signal.

In recent studies, multi-echo gradient recalled echo (mGRE) based MWI (referred here as 'GRE-MWI') has been suggested to separate multi-exponential T_2^* components [3]–[6]. These studies have demonstrated that the mGRE signal can also be separated into multiple components mentioned above. Furthermore, GRE-MWI has potential benefits such as large volume coverage, fast scan time and insensitivity to the inhomogeneity of the transmit field compared to SE-MWI. Despite these advantages, however, GRE-MWI suffers from imaging artifacts (e.g. voxel spread function (VSF) effect [7], [8] and physiological noise [9]) which render the mGRE signal to deviate from the pre-assumed numerical model (e.g. multi-component exponential curves or three component exponential curves). Also, the conventional optimization algorithm to solve multi-component exponential curves which is a nonlinear least squares algorithm, has instability problems regarding initial value selection and local minima [10].

Previously, blind source separation (BSS) techniques have been suggested to separate sources of the MR signal without any explicit model or with minimum prior information [11], [12]. Instead of using numerical models, BSS techniques utilize data-driven properties such as "low rankness" or "sparsity." This allows separating specific signals (e.g. pulsation artifacts in fMRI [11], free water in DWI [13]) that are difficult to specify a numerical model. Among various BSS algorithms, robust principal component analysis (rPCA) has been introduced for separation of background signal

in dynamic MRI [14], on/off-resonance signal representation in multispectral imaging [15] and elimination of MR artifacts [16], [17]. Based on singular value decomposition (SVD) analysis, rPCA extracts redundant signal sources using low-rank property (or fixed-rank property) and encourages the sparsity of the residual signal.

In this study, as an alternative to conventional nonlinear least squares approach, a modified version of rPCA is developed for signal separation in mGRE targeted for MWF mapping. The proposed technique separates mGRE images into two unit-rank components (referred to as $\mathbf{L}_1$ and $\mathbf{L}_2$) and sparse component (referred to as $\mathbf{S}$). In this process, matrix hankelization and non-negative matrix factorization (NMF) are utilized to further enhance the separation of multi-component exponential signals. This offers $\mathbf{L}_1$, $\mathbf{L}_2$, and $\mathbf{S}$ to represent slow-decaying, fast-decaying and artifact components, respectively. An alternative MWF map is suggested as the ratio of $\mathbf{L}_2$ to sum of $\mathbf{L}_1$ and $\mathbf{L}_2$. The proposed technique is demonstrated in healthy volunteers and clinical patients.

The rest of this paper is as follows. In Section II, the conventional model-based GRE-MWI methods are introduced and the motivation of SVD analysis for the mGRE signal is described. In Section III, the modification version of rPCA algorithm is described. The methods and results of the simulation and in-vivo experiments are described in Section IV and V, respectively. Finally, Section VI contains the discussion and conclusion.

II. Background

A. Model-Based MWF Mapping

The multi-component magnitude model fits the decay curve to the following [18]:

$$S(t) = \sum_{j=1}^{M} A_j e^{-(1/T_{2,j}^*)t} \tag{1}$$

where $S(t)$ is the measured signal at time t, A_j is the unknown amplitude of the spectral component with relaxation time $T_{2,j}^*$, M is the number of T_2^* components. Equation (1) is typically solved by regularized non-negative least squares (rNNLS) forming a continuous spectral distribution of T_2^* components [18]. Then, the myelin water component (i.e., fast-decaying signal) and axonal/extracellular water component (i.e., slowly-decaying signal) are separated based on a cutoff T_2^* (e.g. 25ms) value [19], [20].

The three-component magnitude model fits the decay curve to the following:

$$S(t) = A_{my}e^{-(1/T_{2,my}^*)t} + A_{ax}e^{-(1/T_{2,ax}^*)t} + A_{ex}e^{-(1/T_{2,ex}^*)t} \tag{2}$$

where A_{my}, A_{ax} and A_{ex} are the amplitude of the three water components, $T_{2,my}^*$, $T_{2,ax}^*$ and $T_{2,ex}^*$ are T_2^* values of the three water components [6], [20].

Lastly, the three-component complex model fits the decay curve to the following [4]:

$$\begin{aligned} S(t) = (&A_{my}e^{-\left(1/T_{2,my}^* + i2\pi\,\Delta f_{bg+my}\right)t} \\ &+ A_{ax}e^{-\left(1/T_{2,ax}^* + i2\pi\,\Delta f_{bg+ax}\right)t} \\ &+ A_{ex}e^{-(1/T_{2,ex}^* + i2\pi\,\Delta f_{bg+ex})t})e^{-i\varphi_0} \end{aligned} \tag{3}$$

where Δf_{bg+my}, Δf_{bg+ax} and Δf_{bg+ex} are the frequency offset of the three water components plus the sum of background frequency offset, φ_0 is the B_1^+ phase offset.

For the three-component models, Eqs (2) and (3), the parameters are estimated by minimizing the least-squares errors using an iterative nonlinear curve-fitting algorithm [4], [10], [20]. The MWF can be calculated by dividing the myelin water component (i.e., fast-decaying signal) to the total water component. In this approach, the initial values and bounds of the fitting parameters need to be set to avoid getting trapped in local minima (e.g. see [21]).

B. BSS in mGRE Images

We denote matrices by boldface uppercase letters, operators by lightface uppercase letters, vectors by boldface lowercase italics, constants by lightface uppercase italics. $\mathbb{C}$, $\mathbb{R}$ and $\mathbb{R}_+$ represent a set of complex, real and positive-real values, respectively.

Among the various BSS methods, SVD analysis can be performed on the magnitude of mGRE data to separate source signals without any constraint of the signal such as the predetermined model and initial/boundary values.

In order to apply standard SVD, the mGRE data, $m(\cdot)$ is represented to the spatio-temporal Casorati matrix as follows:

$$\mathbf{M}(\boldsymbol{r}, t) = \begin{bmatrix} m(\boldsymbol{r}_1, t_1) & m(\boldsymbol{r}_1, t_2) & \cdots & m(\boldsymbol{r}_1, t_{N_t}) \\ m(\boldsymbol{r}_2, t_1) & m(\boldsymbol{r}_2, t_2) & \cdots & m(\boldsymbol{r}_2, t_{N_t}) \\ \vdots & \vdots & \ddots & \vdots \\ m(\boldsymbol{r}_{N_s}, t_1) & m(\boldsymbol{r}_{N_s}, t_2) & \cdots & m(\boldsymbol{r}_{N_s}, t_{N_t}) \end{bmatrix} \tag{4}$$

where $\mathbf{M} \in \mathbb{R}_+^{N_s \times N_t}$, N_s is the total number of spatial components (i.e. number of pixels) and N_t is the number of temporal components (i.e. number of echoes). The standard SVD of $\mathbf{M}$ is represented as:

$$\mathbf{M} = \mathbf{U}\mathbf{S}\mathbf{V}^{\mathrm{T}} = \sum_{k=1}^{\min\{N_s, N_t\}} \lambda_k \boldsymbol{u}_k \boldsymbol{v}_k^T \tag{5}$$

where $\{\lambda_k\}_{k=1}^{\min\{N_s,N_t\}} \in \mathbb{R}$ are the singular values of $\mathbf{M}$, $\{\mathbf{u}_k\}_{k=1}^{\min\{N_s,N_t\}} \in \mathbb{R}^{\min\{N_s,N_t\}\times 1}$ are the left singular vectors representing the spatial weight, $\{\boldsymbol{v}_k\}_{k=1}^{\min\{N_s,N_t\}} \in \mathbb{R}^{\min\{N_s,N_t\}\times 1}$ are the right singular vectors representing the temporal basis. The rank-R approximation of $\mathbf{M}$ is obtained by:

$$\begin{aligned} \widehat{\mathbf{M}} &= \widehat{\mathbf{U}}\widehat{\mathbf{S}}\widehat{\mathbf{V}}^{\mathrm{T}} = \sum_{k=1}^{R} \lambda_k \boldsymbol{u}_k \boldsymbol{v}_k^T, \\ s.t.\ \left\|\mathbf{M} - \widehat{\mathbf{M}}\right\|_F &= \sqrt{\sum_{k=R+1}^{\min\{N_s,N_t\}} \lambda_k^2} \end{aligned} \tag{6}$$

where $\hat{\mathbf{U}} \in \mathbb{R}^{N_s \times R}$, $\hat{\mathbf{S}} \in \mathbb{R}^{R\times R}$, $\hat{\mathbf{V}} \in \mathbb{R}^{N_t \times R}$, F represents the Frobenius norm. For the example mGRE data used here, the rank was approximated to four where the power of the residual signal is below 2%.

Representative $\{\boldsymbol{u}_k\}_{k=1}^R$ and $\{\boldsymbol{v}_k\}_{k=1}^R$ are shown in Fig.1a. As a result of standard SVD, signal sources are separated into the $\{\boldsymbol{v}_k\}_{k=1}^R$, which is ordered by the redundancy of the source signal. Among the temporal bases in Fig.1a, the first basis, $\boldsymbol{v}_1$, represents a slow-decaying T_2^* relaxation ($T_2^* \approx 44$ms) with relatively homogeneous spatial weights, $\boldsymbol{u}_1$. The other bases, $\boldsymbol{v}_2$, $\boldsymbol{v}_3$, and $\boldsymbol{v}_4$, however, have negative values

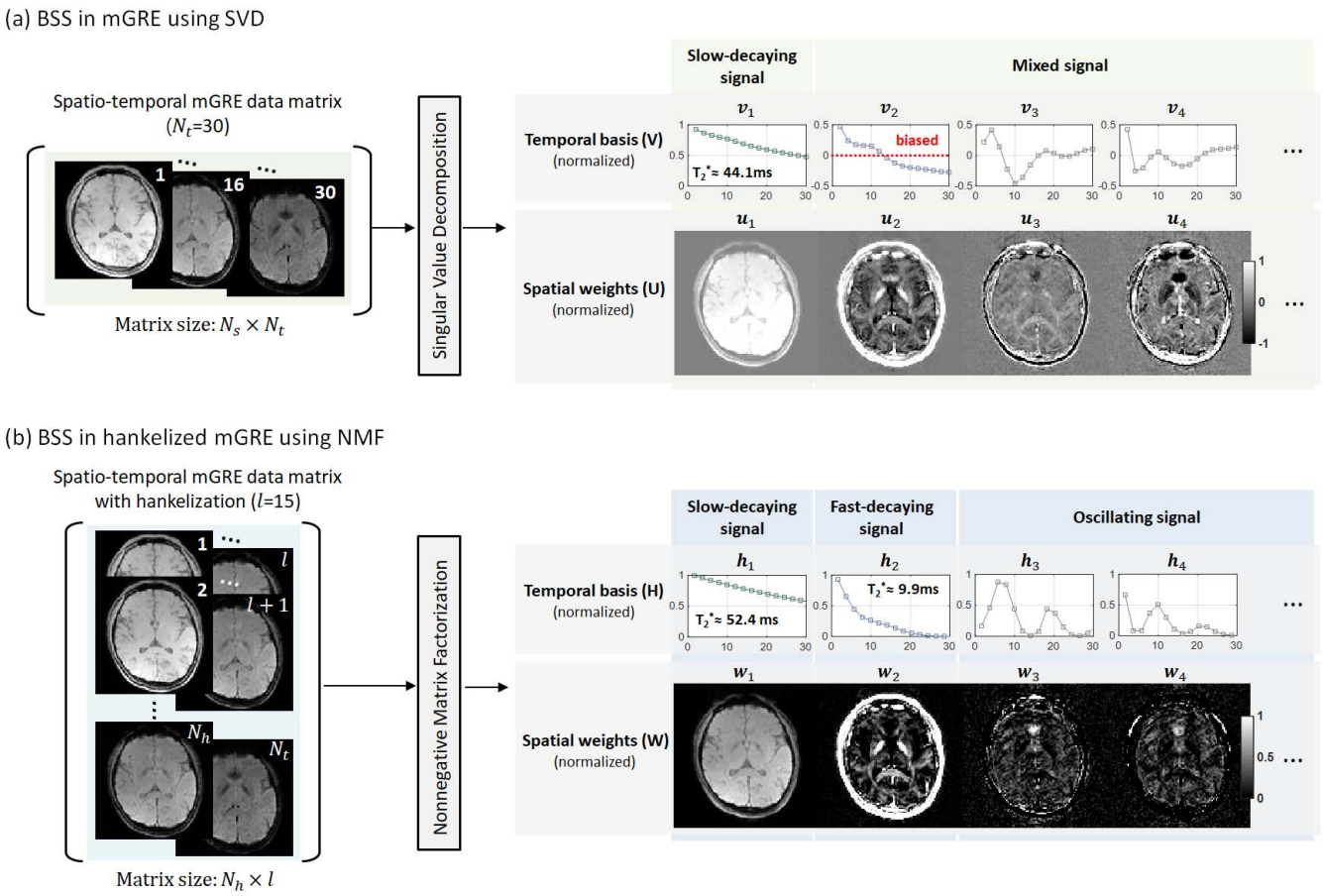

Fig. 1. A conceptual illustration of BSS in spatio-temporal mGRE data matrix (subject 1). (a) Standard SVD applied to mGRE data matrix and (b) NMF applied to mGRE data matrix with hankelization ($\ell = 15$). For each BSS scheme, four representative temporal bases ($\{\boldsymbol{v}_k\}_{k=1}^4$ and $\{\boldsymbol{h}_k\}_{k=1}^4$) and spatial weights ($\{\boldsymbol{u}_k\}_{k=1}^4$ and $\{\boldsymbol{w}_k\}_{k=1}^4$) are shown. Note that BSS using NMF provides temporal bases that corresponds more to the physical signal characteristics than using SVD.

which cannot represent a true tissue-oriented T_2^* relaxation signal. Particularly, $\boldsymbol{v}_2$ represents fast-decaying signal but biased to negative value (Fig. 1a). The reason for this is that real-valued exponential decays (e.g., multi component T_2^* relaxation signals) are highly correlated with each other and separation of these signal sources are badly-conditioned under the constraint of orthogonality. Nevertheless, the spatial weight maps represent different anatomic features for $\boldsymbol{u}_2$, $\boldsymbol{u}_3$, and $\boldsymbol{u}_4$.

Through SVD, we have described the potential of BSS in mGRE data. Although the temporal basis cannot reveal the actual feature of T_2^* relaxation, the signal sources can be distinguished by different characteristics.

III. Theory

A. Priorities of mGRE Signal

In order to overcome the aforementioned problem when using standard SVD, additional constraints in the signal sources were incorporated which enforces the non-negativity of the temporal basis and exponential characteristics of T_2^* relaxation.

As a variant of SVD, non-negative matrix factorization (NMF) was implemented to take into consideration that the T_2^* relaxation of the myelin and axonal/extracellular water components is non-negative [22]. This constraint is similar to a common assumption used in conventional MWI processing (i.e. NNLS) [6]–[19], [20]. The NMF of the spatio-temporal matrix $\mathbf{M}$ is now represented as:

$$\mathbf{M} \approx \widehat{\mathbf{W}}\widehat{\mathbf{H}}^{\mathrm{T}} = \sum_{k=1}^{R} \boldsymbol{w}_k \boldsymbol{h}_k^T \tag{7}$$

where $\widehat{\mathbf{W}} \in \mathbb{R}_+^{N_s \times R}$, $\widehat{\mathbf{H}} \in \mathbb{R}_+^{N_t \times R}$, $\{\boldsymbol{w}_k\}_{k=1}^R \in \mathbb{R}_+^{N_s \times 1}$ are the left singular vectors representing the spatial weight, $\{\boldsymbol{h}_k\}_{k=1}^R \in \mathbb{R}_+^{N_t \times 1}$ are the right singular vectors representing the temporal basis. In conventional NMF, $\widehat{\mathbf{W}}$ and $\widehat{\mathbf{H}}$ are obtained by:

$$\min \left\| \mathbf{M} - \widehat{\mathbf{W}}\widehat{\mathbf{H}}^{\mathrm{T}} \right\|_F^2 \quad s.t.\ \widehat{\mathbf{W}}, \widehat{\mathbf{H}} \geq 0 \tag{8a}$$

$$\mathrm{H} \leftarrow \mathrm{H} \odot \frac{\mathrm{W}^{\mathrm{T}}\mathrm{M}}{\mathrm{W}^{\mathrm{T}}\mathrm{W}\mathrm{H}}, \quad \mathrm{W} \leftarrow \mathrm{W} \odot \frac{\mathrm{X}\mathrm{H}^{\mathrm{T}}}{\mathrm{W}\mathrm{H}\mathrm{H}^{\mathrm{T}}} \tag{8b}$$

using multiplicative update rule with element-wise multiplication operator $\odot$ [23]. As the results of NMF depend on the initial value of $\widehat{\mathbf{W}}$ and $\widehat{\mathbf{H}}$, various initialization techniques have been suggested [24]–[26]. Here, based on the observation of standard SVD in mGRE data which has potential to represent tissue-oriented structure (Fig. 1a), NMF with SVD based initialization method in [24] referred to as nonnegative double singular value decomposition (NNDSVD) was implemented.

One of the features of NNDSVD is that the uniqueness of initial value guarantee the convergence to the same solution [24].

Prior to the NMF operation, as a temporal operator, hankelization was implemented in order to enforce the unit rank property of each temporal basis [27]. The hankelized matrix of $\mathbf{M}$ with hankelization length l is shown in Fig.1b and is represented as [28], [29]:

$$\mathcal{H}_l\left(\mathbf{M}\left(\boldsymbol{r},t\right)\right) = \begin{bmatrix} m\left(\boldsymbol{r}_1,t_1\right) & m\left(\boldsymbol{r}_1,t_2\right) & \cdots & m\left(\boldsymbol{r}_1,t_l\right) \\ m\left(\boldsymbol{r}_1,t_2\right) & m\left(\boldsymbol{r}_1,t_3\right) & \cdots & m\left(\boldsymbol{r}_1,t_{l+1}\right) \\ \vdots & \vdots & \ddots & \vdots \\ m\left(\boldsymbol{r}_{N_h},t_1\right) & m\left(\boldsymbol{r}_{N_h},t_2\right) & \cdots & m\left(\boldsymbol{r}_{N_h},t_{N_t}\right) \end{bmatrix} \tag{9}$$

where $\mathcal{H}_l(\mathbf{M}) \in \mathbb{R}_+^{N_h \times l}$ and $N_h = N_s(N_t - l + 1)$. When the echo spacing is equidistant (i.e., $t_i - t_{i-1} = \Delta TE$), the relaxation rate for the j^{th} component in Eq. (1) is proportional by an amount $e^{-(1/T_{2,j}^*)\Delta TE}$ for any echo time. This indicates that the hankelization of a mono-exponential signal has unit-rank. Based on this, we implemented the hankelization to encourage the unit-rank property of each exponential decay [27]. The hankelization length, l, was selected to half the total number of echoes as an optimal length for exponential signal [30].

After incorporating these two constraints (Fig.1b), the first and second temporal basis, $\boldsymbol{h}_1$ and $\boldsymbol{h}_2$, become closer to pure exponential decays. The separated mono-exponential T_2^* values corresponds well to the slow (i.e., axonal/extracellular water signal) and fast (i.e., myelin water signal) components (T_2^* of $\boldsymbol{h}_1 = 52.4$ms, T_2^* of $\boldsymbol{h}_2 = 9.9$ms) [6]. Furthermore, the other temporal bases, $\boldsymbol{h}_3$ and $\boldsymbol{h}_4$, represent oscillating signals which are related to remnant residual components including artifacts.

B. Algorithm of the Proposed rPCA-MWF

Based on the aforementioned ideas, a modified rPCA to separate three distinct sources from mGRE data is presented. The original rPCA separates the signal sources into a low-rank component, $\mathbf{L}$, and a sparse component, $\mathbf{S}$, by solving the minimization problem with convex objective function as [16], [31]:

$$\mathcal{J}\left(\mathbf{L},\mathbf{S}\right) \equiv \frac{1}{2}\left\|\mathbf{L}+\mathbf{S}-\mathbf{M}\right\|_2^2 + \mu\left\|\mathbf{L}\right\|_* + \rho\left\|\mathbf{S}\right\|_1 \tag{10}$$

where $\mathbf{M},\mathbf{L},\mathbf{S} \in \mathbb{R}^{N_s \times N_t}$, $\|\cdot\|_*$ denotes the nuclear norm, $\|\cdot\|_1$ denotes the ℓ_1-norm, μ and ρ denote regularization parameters for low rankness and sparsity, respectively. In this study, the signal source of mGRE data was separated to two unit-rank components (i.e., slow-decaying signal ($\mathbf{L}_1$) and fast-decaying signal ($\mathbf{L}_2$)) and sparse component (i.e., residual artifact signal ($\mathbf{S}$)). The minimization problem $\min_{\mathbf{L}_1,\mathbf{L}_2,\mathbf{S}} \mathcal{J}(\mathbf{L}_1,\mathbf{L}_2,\mathbf{S})$ with the convex objective function is defined as:

$$\begin{aligned}\mathcal{J}\left(\mathbf{L}_1,\mathbf{L}_2,\mathbf{S}\right) \equiv\ & \frac{1}{2}\left\|\mathbf{L}_1+\mathbf{L}_2+\mathbf{S}-\mathbf{M}\right\|_2^2 \\ & + \mu_1\sum\nolimits_{\mathrm{r}}\left\|\mathcal{R}_r\left(\mathcal{H}_l\left(\mathbf{L}_1\right)\right)\right\|_* \\ & + \mu_2\sum\nolimits_{\mathrm{r}}\left\|\mathcal{R}_r\left(\mathcal{H}_l\left(\mathbf{L}_2\right)\right)\right\|_* + \rho\left\|\Psi\left(\mathbf{S}\right)\right\|_1\end{aligned} \tag{11}$$

where $\mathcal{H}_l$ denotes hankelization operator in the temporal domain, Ψ denotes temporal sparsifying operater (1D FFT in the echo domain), $\mathcal{R}_r$ denotes the extraction of local patches for locally low-rank (LLR) structure at the r^{th} patch [32]–[34], μ_1, μ_2 and ρ denote regularization parameters for LLR and sparsity respectively. The LLR constraint, which has higher redundancy than entire image, was implemented to encourage the low rankness of local patches for $\mathbf{L}_1$ and $\mathbf{L}_2$ [32]–[34]. Equation (11) is solved using the alternating direction method of multipliers (ADMM) [35]–[37]. Based on the variable splitting scheme in [36], Eq (11) is re-formulated as:

$$\begin{aligned}\min_{\substack{\mathbf{U}_{1,\mathbf{r}},\mathbf{U}_{2,\mathbf{r}},\mathbf{U}_3 \\ \mathbf{L}_1,\mathbf{L}_2,\mathbf{S}}}\ & \frac{1}{2}\left\|\mathbf{L}_1+\mathbf{L}_2+\mathbf{S}-\mathbf{M}\right\|_2^2 \\ & +\mu_1\sum\nolimits_r\left\|\mathbf{U}_{1,\mathrm{r}}\right\|_* + \mu_2\sum\nolimits_r\left\|\mathbf{U}_{2,\mathrm{r}}\right\|_* + \rho\left\|\mathbf{U}_3\right\|_1 \\ s.t.\ & \begin{cases}\mathbf{U}_{1,\mathrm{r}} = \mathcal{R}_r\left(\mathcal{H}_l\left(\mathbf{L}_1\right)\right) \\ \mathbf{U}_{2,\mathrm{r}} = \mathcal{R}_r\left(\mathcal{H}_l\left(\mathbf{L}_2\right)\right) \\ \mathbf{U}_3 = \Psi\left(\mathbf{S}\right)\end{cases}\end{aligned} \tag{12}$$

and the associated augmented Lagrangian function is:

$$\begin{aligned}\mathcal{L}_A =\ & \frac{1}{2}\left\|\mathbf{L}_1+\mathbf{L}_2+\mathbf{S}-\mathbf{M}\right\|_2^2 \\ & +\mu_1\sum\nolimits_r\left\|\mathbf{U}_{1,\mathrm{r}}\right\|_* + \mu_2\sum\nolimits_r\left\|\mathbf{U}_{2,\mathrm{r}}\right\|_* + \rho\left\|\mathbf{U}_3\right\|_1 \\ & +\sum\nolimits_r\left\langle\mathbf{Z}_{1,r},\mathcal{R}_r\left(\mathcal{H}_l\left(\mathbf{L}_1\right)\right)-\mathbf{U}_{1,r}\right\rangle \\ & +\sum\nolimits_r\left\|\frac{\delta_1}{2}\mathcal{R}_r\left(\mathcal{H}_l\left(\mathbf{L}_1\right)\right)-\mathbf{U}_{1,\mathrm{r}}\right\|_2^2 \\ & +\sum\nolimits_r\left\langle\mathbf{Z}_{2,r},\mathcal{R}_r\left(\mathcal{H}_l\left(\mathbf{L}_2\right)\right)-\mathbf{U}_{2,r}\right\rangle \\ & +\sum\nolimits_r\left\|\frac{\delta_2}{2}\mathcal{R}_r\left(\mathcal{H}_l\left(\mathbf{L}_2\right)\right)-\mathbf{U}_{2,\mathrm{r}}\right\|_2^2 \\ & +\left\langle\mathbf{Z}_3,\Psi\left(\mathbf{S}\right)-\mathbf{U}_3\right\rangle + \frac{\delta_3}{2}\left\|\Psi\left(\mathbf{S}\right)-\mathbf{U}_3\right\|_2^2\end{aligned} \tag{13}$$

where $\mathbf{Z}_{1,\mathrm{r}}$,$\mathbf{Z}_{2,\mathrm{r}}$ and $\mathbf{Z}_3$ are Lagrangian multipliers. Ignoring constants irrelevant to optimization, Eq (13) can be written as:

$$\begin{aligned}\mathcal{L}_A =\ & \frac{1}{2}\left\|\mathbf{L}_1+\mathbf{L}_2+\mathbf{S}-\mathbf{M}\right\|_2^2 \\ & +\mu_1\sum\nolimits_r\left\|\mathbf{U}_{1,\mathrm{r}}\right\|_* + \mu_2\sum\nolimits_r\left\|\mathbf{U}_{2,\mathrm{r}}\right\|_* + \rho\left\|\mathbf{U}_3\right\|_1 \\ & +\sum\nolimits_r\frac{\delta_1}{2}\left\|\mathcal{R}_r\left(\mathcal{H}_l\left(\mathbf{L}_1\right)\right)+\delta_1^{-1}\mathbf{Z}_{1,\mathrm{r}}-\mathbf{U}_{1,\mathrm{r}}\right\|_2^2 \\ & +\sum\nolimits_r\frac{\delta_2}{2}\left\|\mathcal{R}_r\left(\mathcal{H}_l\left(\mathbf{L}_2\right)\right)+\delta_2^{-1}\mathbf{Z}_{2,\mathrm{r}}-\mathbf{U}_{2,\mathrm{r}}\right\|_2^2 \\ & +\frac{\delta_3}{2}\left\|\Psi\left(\mathbf{S}\right)-\delta_3^{-1}\mathbf{Z}_3-\mathbf{U}_3\right\|_2^2\end{aligned} \tag{14}$$

where δ_1, δ_2, δ_3 denotes regularization parameters. The ADMM minimizes $\mathcal{L}_A$ over $\mathbf{U}_1,\mathbf{U}_2,\mathbf{U}_3,\mathbf{L}_1,\mathbf{L}_2$ and $\mathbf{S}$ separately by solving sub-problems with closed-form solutions:

$$\begin{aligned}\mathbf{U}_{1,\mathrm{r}}^{(k+1)} =\ & \operatorname*{argmin}_{\mathbf{U}_{1,\mathrm{r}}}\frac{\mu_1}{\delta_1}\left\|\mathbf{U}_{1,\mathrm{r}}\right\|_* \\ & +\frac{1}{2}\left\|\mathcal{R}_r\left(\mathcal{H}_l\left(\mathbf{L}_1^{(k)}\right)\right)+\delta_1^{-1}\mathbf{Z}_{1,\mathrm{r}}^{(k)}-\mathbf{U}_{1,\mathrm{r}}\right\|_2^2 \\ =\ & SVT_{\mu_1/\delta_1}\left(\mathcal{R}_r\left(\mathcal{H}_l\left(\mathbf{L}_1^{(k)}\right)\right)+\delta_1^{-1}\mathbf{Z}_{1,\mathrm{r}}^{(k)}\right)\end{aligned} \tag{15a}$$

$$\mathbf{U}_{2,\mathrm{r}}^{(k+1)} = \underset{\mathbf{U}_{2,\mathrm{r}}}{\operatorname{argmin}} \frac{\mu_2}{\delta_2} \left\|\mathbf{U}_{2,\mathrm{r}}\right\|_* + \frac{1}{2}\left\|\mathcal{R}_r\left(\mathcal{H}_l\left(\mathbf{L}_2^{(k)}\right)\right) + \delta_2^{-1}\mathbf{Z}_{2,\mathrm{r}}^{(k)} - \mathbf{U}_{2,\mathrm{r}}\right\|_2^2 = SVT_{\mu_2/\delta_2}\left(\mathcal{R}_r\left(\mathcal{H}_l\left(\mathbf{L}_2^{(k)}\right)\right) + \delta_2^{-1}\mathbf{Z}_{2,\mathrm{r}}^{(k)}\right) \quad (15b)$$

$$\mathbf{U}_3^{(k+1)} = \underset{\mathbf{U}_3}{\operatorname{argmin}} \frac{\rho}{\delta_3}\left\|\mathbf{U}_3\right\|_1 + \frac{1}{2}\left\|\mathbf{S}^{(k)} + \delta_3^{-1}\mathbf{Z}_3^{(k)} - \mathbf{U}_3\right\|_2^2 = ST_{\rho/\delta_3}(\mathbf{S}^{(k)} + \delta_3^{-1}\mathbf{Z}_3^{(k)}) \quad (15c)$$

where SVT_{μ_1/δ_1} and SVT_{μ_2/δ_2} denotes (hard) singular value thresholding operators using NMF for each local patches r, ST_{ρ/δ_3} denotes soft thresholding operators [31], [38].

$$\mathbf{L}_1^{(k+1)} = \underset{\mathbf{L}_1}{\operatorname{argmin}} \frac{1}{2}\left\|\mathbf{L}_1 + \mathbf{L}_2^{(k)} + \mathbf{S}^{(k)} - \mathbf{M}\right\|_2^2 + \sum\nolimits_r \frac{\delta_1}{2}\left\|\mathcal{R}_r\left(\mathcal{H}_l\left(\mathbf{L}_1\right)\right) + \delta_1^{-1}\mathbf{Z}_{1,\mathrm{r}}^{(k)} - \mathbf{U}_{1,\mathrm{r}}^{(k)}\right\|_2^2 = \frac{1}{1+\delta_1}(\mathbf{M} - \mathbf{L}_2^{(k)} - \mathbf{S}^{(k)} + \delta_1\mathbf{U}_1 - \mathbf{Z}_1) \quad (16a)$$

$$\mathbf{L}_2^{(k+1)} = \underset{\mathbf{L}_2}{\operatorname{argmin}} \frac{1}{2}\left\|\mathbf{L}_1^{(k+1)} + \mathbf{L}_2 + \mathbf{S}^{(k)} - \mathbf{M}\right\|_2^2 + \sum\nolimits_r \frac{\delta_2}{2}\left\|\mathcal{R}_r\left(\mathcal{H}_l\left(\mathbf{L}_2\right)\right) + \delta_2^{-1}\mathbf{Z}_{2,\mathrm{r}}^{(k)} - \mathbf{U}_{2,\mathrm{r}}^{(k)}\right\|_2^2 = \frac{1}{1+\delta_2}(\mathbf{M} - \mathbf{L}_1^{(k+1)} - \mathbf{S}^{(k)} + \delta_2\mathbf{U}_2 - \mathbf{Z}_2) \quad (16b)$$

$$\mathbf{S}^{(k+1)} = \underset{\mathbf{S}}{\operatorname{argmin}} \frac{1}{2}\left\|\mathbf{L}_1^{(k+1)} + \mathbf{L}_2^{(k+1)} + \mathbf{S} - \mathbf{M}\right\|_2^2 + \frac{\delta_3}{2}\left\|\Psi\left(\mathbf{S}\right) - \delta_3^{-1}\mathbf{Z}_3^{(k)} - \mathbf{U}_3^{(k)}\right\|_2^2 = \frac{1}{1+\delta_3}(\mathbf{M} - \mathbf{L}_1^{(k+1)} - \mathbf{L}_2^{(k+1)} + \delta_3\mathbf{U}_3 - \mathbf{Z}_3) \quad (16c)$$

where dehankelization was performed while solving Eq (16a) and Eq (16b). Corresponding Lagrangian multipliers are updated as:

$$\mathbf{Z}_1^{(k+1)} = \mathbf{Z}_1^{(k)} + \mathbf{L}_1^{(k+1)} - \mathbf{U}_1^{(k+1)} \quad (17a)$$

$$\mathbf{Z}_2^{(k+1)} = \mathbf{Z}_2^{(k)} + \mathbf{L}_2^{(k+1)} - \mathbf{U}_2^{(k+1)} \quad (17b)$$

$$\mathbf{Z}_3^{(k+1)} = \mathbf{Z}_3^{(k)} + \Psi\left(\mathbf{S}^{(k+1)}\right) - \mathbf{U}_3^{(k+1)}. \quad (17c)$$

The regularization parameters for the proposed rPCA-MWF were empirically set as follows: $\mu_1 = 1, \mu_2 = 1, \rho = 0.5$, $\delta_1 = 0.01, \delta_2 = 0.01, \delta_3 = 0.0005$. The local patch size and convergence tolerance were empirically set as follows: patch size $= 8\times8\times8$, and $\epsilon = 10^{-6}$. Here, the convergence rate was estimated to relative residual ($\left\|\mathbf{X}^{k+1} - \mathbf{X}^{k}\right\|_2 / \left\|\mathbf{X}^{k}\right\|_2 \times 100$). A summary of the iteration process is described in Table 1. (See supplementary materials (Fig. S1) for simulations on the determination of hyperparameters and the convergence rate of the algorithm).

Afterwards, the MWF was mapped as the ratio of 2nd unit rank component to total unit-rank component at TE_1 for each voxel;

$$MWF\left(\boldsymbol{r}\right) = \frac{\mathbf{L}_2\left(\boldsymbol{r}, TE_1\right)}{\mathbf{L}_1\left(\boldsymbol{r}, TE_1\right) + \mathbf{L}_2\left(\boldsymbol{r}, TE_1\right)} \times 100(\%) \quad (18)$$

TABLE I
rPCA-MWF ALGORITHM

Task:
Find $\mathbf{L}_1$, $\mathbf{L}_2$ and $\mathbf{S}$ minimizing Eq. (11)
Initialization:
Iteration index: $k = 1$,
Initial solutions: $\mathbf{U}_{1,\mathrm{r}}{}^{(0)}, \mathbf{U}_{2,\mathrm{r}}{}^{(0)}, \mathbf{U}_3{}^{(0)} = 0$,
$\mathbf{L}_1 = SVT_{\mu_1/\delta_1}(\mathbf{M})$,
$\mathbf{L}_2 = SVT_{\mu_2/\delta_2}(\mathbf{M}) - \mathbf{L}_1$,
$\mathbf{S} = \mathbf{M} - \mathbf{L}_1 - \mathbf{L}_2$,
$\mathbf{Z}_1{}^{(0)}, \mathbf{Z}_2{}^{(0)}, \mathbf{Z}_3{}^{(0)} = 0$,
while "not converged" **and** "k < 100" **do**
Step 1: Update $\mathbf{U}_1, \mathbf{U}_2, \mathbf{U}_3$ by solving Eq. (15)
Step 2: Update $\mathbf{L}_1, \mathbf{L}_2, \mathbf{S}$ by solving Eq. (16)
Step 3: Update $\mathbf{Z}_1, \mathbf{Z}_2, \mathbf{Z}_3$ by solving Eq. (17)
Step 4: Increase the iteration number k
end
Output: $\widehat{\mathbf{L}_1} = \mathbf{L}_1^{\mathrm{k}}$, $\widehat{\mathbf{L}_2} = \mathbf{L}_2^{\mathrm{k}}$, $\widehat{\mathbf{S}} = \mathbf{S}^{\mathrm{k}}$

The residual signal was mapped to the sparse component, which can also be sparsified in the frequency domain.

We provide the source code and related data (in MATLAB) to reproduce most of the results described in this paper. The source code and related data can be downloaded from: https://github.com/Yonsei-MILab.

IV. METHODS

A. Comparison of Model-Based MWF and rPCA-MWF

Among the GRE-MWI models, two types of model-based method were adopted; three-component magnitude and complex model which we refer here as "magnitude model-based" (Eq. (2)) and "complex model-based" (Eq. (3)) respectively. In simulations, magnitude model-based MWF was compared to rPCA-MWF due to difficulty of modeling three component complex signals. In in-vivo experiments, magnitude and complex model-based MWF were compared to rPCA-MWF. In this study, a total 30 echoes were used with the last echo time of 31.81 ms. Note that multi-component magnitude model-based MWF using rNNLS does not provide adequate results due to the limited number of echoes.

B. Simulations

Numerical simulations were performed on an analytic phantom to compare the performance of MWF estimation between model-based MWF and rPCA-MWF for various situations. An analytic phantom composed of 24 region-of-interests (ROI) was designed. Each ROI had a size of 8x8 voxels, containing two water pools (i.e., slowly-decaying component ($T_{2,\mathrm{slow}}^*$) and fast-decaying component ($T_{2,\mathrm{fast}}^*$)) with various T_2^* and MWF (Fig. 2a). The index of each ROI was set to 1-6, 7-12, 13-18 and 19-24 for each column. For ROI 1-12, $T_{2,\mathrm{slow}}^*$ and $T_{2,\mathrm{fast}}^*$ were set to 60ms and 10ms respectively and MWF varied from 2% to 24 % with step size 2%. For ROI 13-18, $T_{2,\mathrm{slow}}^*$ varied from 40ms to 90ms with step size 10ms and $T_{2,\mathrm{S}}^*$ was set to 10ms. For ROI 19-24, $T_{2,\mathrm{slow}}^*$ was set to 60ms and $T_{2,\mathrm{fast}}^*$ varied from 5ms to 15ms with step size 2ms. The MWF

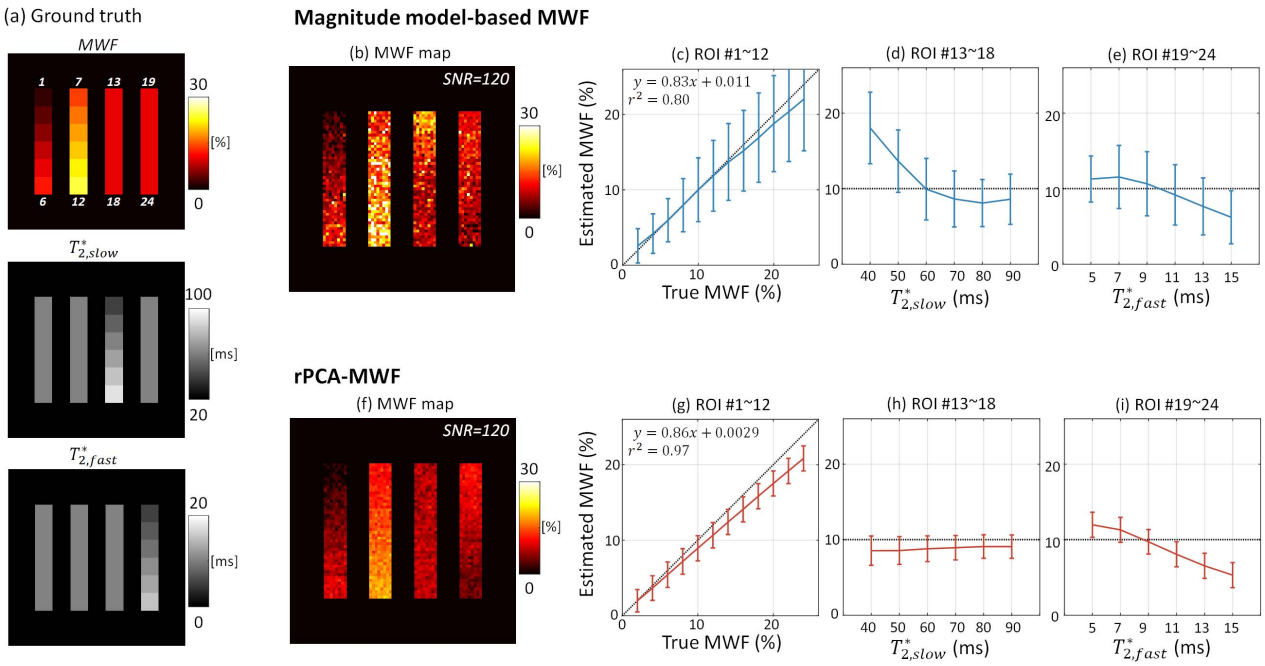

Fig. 2. Numerical simulation of the MWF mapping for various $T^*_{2,\text{slow}}$, $T^*_{2,\text{fast}}$, and MWF. (a) Ground truth of the MWF, $T^*_{2,\text{slow}}$, $T^*_{2,\text{fast}}$. The MWF map and ROI analysis using (b-e) magnitude model-based MWF and (f-i) rPCA-MWF. Each column of ground truth indicates the ROI index 1 ∼ 6, 7 ∼ 12, 13 ∼ 18 and 19 ∼ 24 respectively.

of ROI 13-24 were set to 10%. Each parameter was set based on the literature values of the myelin and axonal/extracellular water component of healthy white matter at 3T [19].

In order to reflect a more realistic biological tissue characteristics representing a continuous distribution for each water pool, the aforementioned T_2^* components of each ROI were modeled to have a Gaussian distribution centered at each T_2^*, with a standard deviation of 10% of each T_2^* [39]. The first TE and echo spacing was set to 2ms and 1ms respectively and 30 echoes were assumed to be sampled [40].

White Gaussian noise was added so that the SNR of the magnitude image at the first TE varied from 240 to 60 with a step size of 20. A series of Monte-Carlo simulations were performed with 100 repetitions for each case. The error of the estimated MWF map was evaluated with RMSE and the standard deviation of each ROI was calculated.

The effects of the number of echoes on the rPCA-MWF was studied using simulated data. The true and estimated MWF was calculated assuming different number of echoes collected (from 12 to 32 with step size of 4). Subsequently, a linear regression of the calculated result was performed. By doing this, the slope of the linear regression provided information about the overall underestimation and the intercept of the regression provided the overall bias information.

C. In-Vivo Experiment

All MR imaging experiments were performed on 3 Tesla clinical scanners (Tim Trio/Skyra, Siemens, Erlangen, Germany or Signa, General Electric Company, Milwaukee, WI). All examination was performed with approval from the institution's ethical review board and all subjects provided signed, informed consent prior to participation. A 12-channel phased-array head coil and a 32-channel head coil were used for data reception in Siemens scanner and GE scanner respectively.

The 3D mGRE imaging parameters were FOV = 256 × 256 × 80mm^3, spatial resolution = 2×2×2 mm^3, TR = 46 ms, TE_1 = 1.65 ms, ΔTE = 1.04 ms, # of echoes = 30, flip-angle = 20°, bandwidth = 1560 Hz/pixel and total scan time = 3min 55sec. For anatomical reference, T_1-weighted sagittal 3D MPRAGE (1.0 mm isotropic) was used for all subjects.

Data were collected from 10 subjects. Subjects 1 ∼ 7 were healthy volunteers (age range: 25-35) with no documented disease in the brain. Subject 8, 9 and 10 were patients with pathologically confirmed disease by a radiologist; dementia (female, age 70), non-amnestic mild cognitive impairment (MCI) disease (female, age 81) and x-linked adrenoleukodystrophy (X-ALD) disease, respectively. Note that all the experiments were performed on Siemens scanner except for subject 10. The experiment for subject 10 with X-ALD disease was performed on GE scanner in order to acquire another quantitative myelin water imaging method equipped on scanner; quantitative inhomogeneous magnetization transfer imaging [41].

For subject 10 with X-ALD, parameters of mGRE imaging were modified due to different scanner conditions: FOV = 256 × 256 × 100mm3, spatial resolution = 1.6×1.6×2.0 mm3, TR = 60 ms, TE_1 = 1.4 ms, ΔTE = 2.1 ms, # of echoes = 16, flip-angle = 25° and scan time = 8min. For anatomical reference, T_1-weighted sagittal image was acquired using 3D FSPGR. Furthermore, a inhomogeneous magnetization transfer (ihMT) imaging protocol [41] was added with the following parameters: 3D SPGR sequence, spatial resolution = 3×3×3 mm3, TR = 10.2 ms, TE = 2 ms, flip-angle = 8° and scan time = 5min 34sec. After data acquisition, quantitative

ihMT (qihMT) map was estimated by taking the difference of the longitudinal relaxation rates between two MT states, dual frequency and single frequency, by using a prototype image processing software provided by GE [41].

The reproducibility was calculated using Pearson's correlation coefficient for white matter region. First, to evaluate the reproducibility of the MWF maps, subjects 1∼7 were scanned twice and a correlation between the two scans was calculated. Student's t-test was performed to evaluate the statistical significance of model-free MWF map against model-based MWF maps. The significance level was set to 0.05. Second, to evaluate the noise sensitivity of the technique, additional white gaussian noise was added to mGRE data from subject 7. The MWF map from original mGRE images was used as a reference. The SNR of the reference mGRE image at the first echo was 160 and the noise corrupted images was from 60 to 140 with step size 20. The correlation between reference and noise additive cases was calculated.

V. Results

A. Simulation

The simulation result of the MWF mapping is shown in Fig. 2. The noise of MWF map was reduced in rPCA-MWF compared to model-based MWF (Fig. 2b and 2f). The standard deviation (STD) of the estimated MWF values from each ROI was reduced by more than 40 % in rPCA-MWF compared to model-based MWF (Fig. 2c-2e and 2g-2i). For the ROIs with varying MWF (i.e., #1∼12), the correlation coefficient of the estimated MWF for true MWF was 20% higher in rPCA-MWF than model-based MWF. However, the linear regression of the estimated MWF showed underestimation of 15% for rPCA-MWF and model-based MWF (Fig. 2c and 2g). Meanwhile, for the ROIs with varying $T^*_{2,\text{slow}}$ and $T^*_{2,\text{fast}}$ (i.e., ROI #13∼24), the accuracy of the estimated MWF was more sensitive to variations in $T^*_{2,\text{fast}}$ than to $T^*_{2,\text{slow}}$ (Fig. 2d-2e and 2h-2i).

The noise sensitivity of estimated MWF values from six representative ROIs is shown in Fig. 3. The six representative ROIs were selected from regions where true MWF, $T^*_{2,\text{slow}}$ and $T^*_{2,\text{fast}}$ have minimum and maximum values (Fig. 2a). The RMSE between true MWF map and estimated MWF map was reduced by more than 40% in rPCA-MWF compared to model-based MWF (Fig. 3a). The STD of rPCA-MWF was invariant against true MWF, $T^*_{2,\text{slow}}$ and $T^*_{2,\text{fast}}$. However, the STD of model-based MWF increased as true MWF increased (Fig. 3b). This shows the sensitivity of model-based method against true MWF. For all range of SNR, rPCA-MWF showed reduced RMSE and STD compared to model-based MWF, which supports robustness against noise of proposed method.

The effect of the number of echoes on the rPCA-MWF is shown in Fig. 4. For both model-based MWF and rPCA-MWF, the overall underestimation gradually decreased as the number of echoes increased (Fig. 4a). Meanwhile, the overall bias decreased as the number of echoes increased for model-based MWF while it was consistent for rPCA-MWF (Fig. 4b). The number of echoes collected was determined to be 30

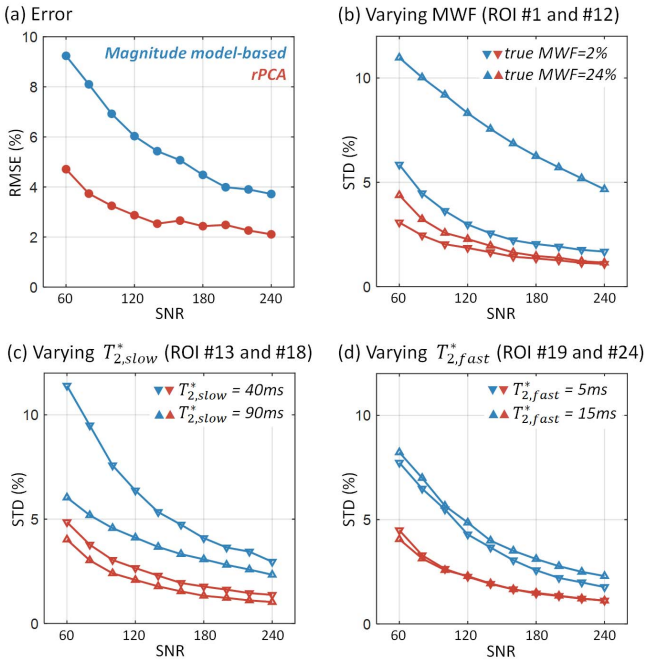

Fig. 3. Noise sensitivity of the MWF map in simulation. (a) RMSE according to SNR. The STD of each ROI for (b) varying MWF (c) varying $T^*_{2,\text{slow}}$ and (c) varying $T^*_{2,\text{fast}}$. Note that only ROI #1,12,13,18,19 and 24 are represented here.

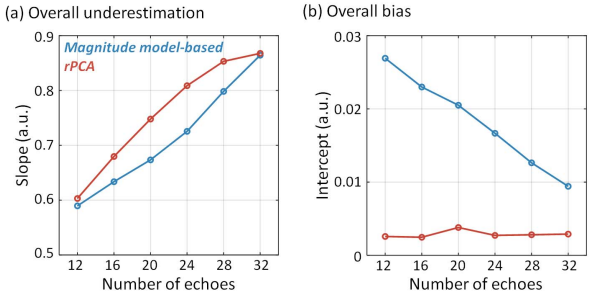

Fig. 4. Effect of number of echoes on the MWF using simulated data. (a) The slope and (b) the intercept following linear regression of Fig. 2c and 2g for varying number of echoes. Note that the slope represents overall underestimation and the intercept represents overall bias.

(i.e., the last echo of 32 ms) since the underestimation tended to slow down at this value while maintaining scan time. Additionally, the accuracy of estimated MWF values from four representative ROIs is shown in Fig. S2. The four representative ROIs were selected from regions where true $T^*_{2,\text{slow}}$ and $T^*_{2,\text{fast}}$ have minimum and maximum values. The accuracy of rPCA-MWF outperformed for varying $T^*_{2,\text{slow}}$.

B. In-Vivo Experiments

Component-wise analysis for the decomposed source signal is shown in Fig. 5. The decomposed mGRE data matrix using proposed rPCA-MWF shows three components; $\mathbf{L}_1$, $\mathbf{L}_2$ and $\mathbf{S}$. The $\mathbf{L}_1$ component represents slow-varying signals, while the $\mathbf{L}_2$ component represents signals appearing only at early echoes. The R^*_2 maps of $\mathbf{M}$, $\mathbf{L}_1$ and $\mathbf{L}_2$ were reconstructed by mono-exponential fitting and the histogram of T^*_2 measurements were plotted after removing the skull region by using FSL BET [42] (Fig. 5b and 5c). The mean T^*_2

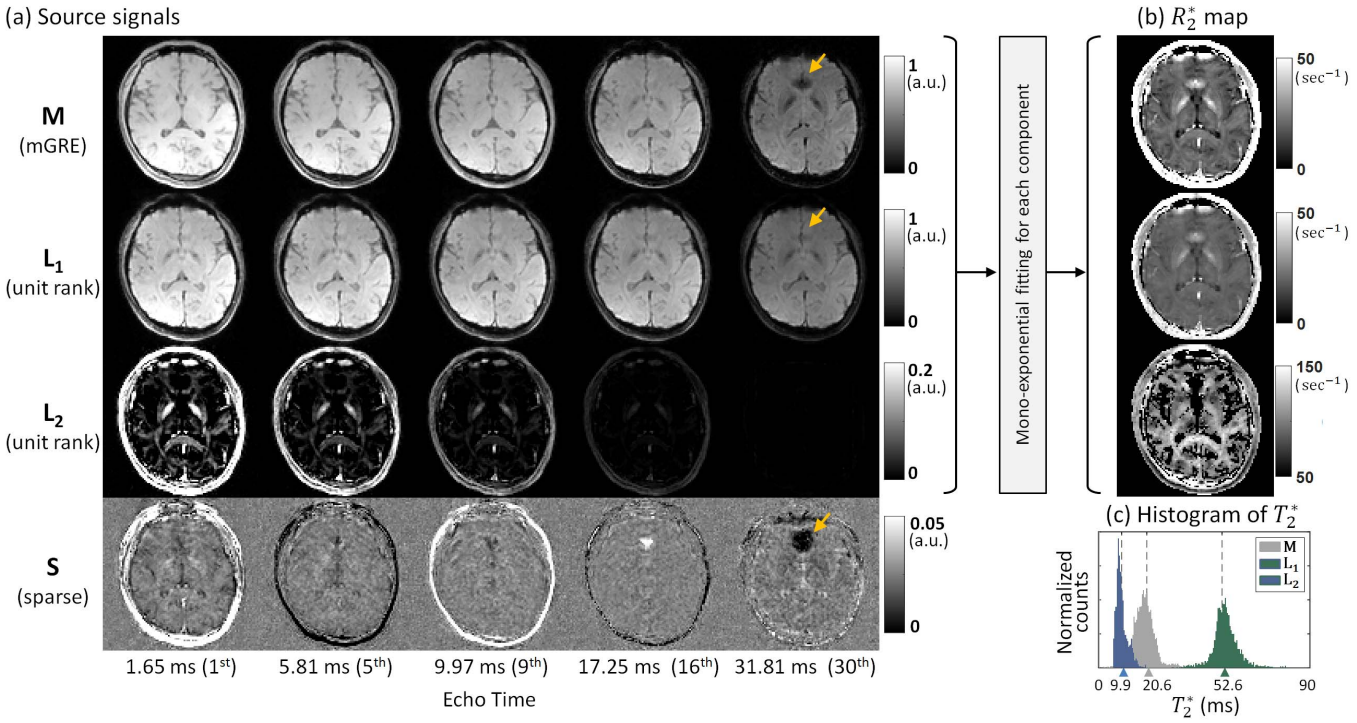

Fig. 5. Component-wise analysis of rPCA-MWF (subject 1). (a) Spatial distribution and temporal evolution of original mGRE and each decomposed component for five representative echo times. Note that the abnormal signal decay at frontal lobe of **M** is decomposed to **S** component (yellow arrow). (b) R_2^* map estimated by mono-exponential fitting of **M**, $\mathbf{L}_1$ and $\mathbf{L}_2$ signals. (c) Histogram of T_2^* from each R_2^* map. Note that the T_2^* of $\mathbf{L}_1$ and $\mathbf{L}_2$ are not biased to a single T_2^* but represent various T_2^*.

TABLE II
REPRODUCIBILITY ANALYSIS OF THE MWF MAP FOR 7 HEALTHY VOLUNTEERS

	Magnitude model-based	Complex model-based	**rPCA**
r^2 (a.u.)	0.802 *	0.812 *	**0.925**
std (a.u.)	0.087	0.072	**0.052**

r^2: Pearson's correlation coefficient, * $p < 0.05$

values were measured at 20.6ms, 52.6ms and 9.7ms while the mean amplitude was 0.91, 0.84 and 0.08, respectively. The T_2^* measurements, especially short T_2^* value, corresponded well to the literature values of GRE-MWI reported to being 6∼15 ms [3], [8], [20]. The **S** component represented residual signals including noise, and B_0–oriented artifact (frontal lobe, yellow arrow in Fig. 5a). Other tissue signals such as subcutaneous fat is not of interest in this study.

Representative MWF maps using magnitude model-based, complex model-based and rPCA technique are shown in Fig. 6. A clearer visualization of the white matter area is noted for rPCA-MWF and corresponds well to the details of the MPRAGE images. Note that the magnitude model-based MWF and rPCA-MWF shows overestimation in the globus pallidus region compared to complex model-based MWF (first slice in Fig. 6).

Reproducibility results for the 7 subjects is given in Table II. Correlation coefficients between two repeated scans are largest in the rPCA-MWF map with 0.925, which corresponds to an improvement of more than 10% compared to model-based MWF map ($p<0.05$). Also, the STD was smallest for the rPCA-MWF. In Fig.7, reproducibility analysis with respect to noise is shown. As more noise is present, the model-based MWF maps show reduced reproducibility with correlation coefficient under 0.8. The rPCA-MWF shows robustness with correlation coefficient over 0.9 even at SNR of 60. The discrete variation of rPCA-MWF resulted from the mis-estimation of $\mathbf{L}_2$ after SNR of 80.

Cases when artifacts were present are shown in Fig. 8. Subject 9, 8 and 6 showed B_0 inhomogeneity, motion artifact and zipper artifact corrupted cases respectively. In Fig. 8a, temporal signal evolution of mGRE deviated from the exponential decay at the frontal lobe, and the complex model-based MWF image presented abnormal high values. The rPCA-MWF removed this to the **S** component. In Fig. 8b, the aliasing patterns in mGRE image are separated to the S component and rPCA-MWF shows a more uniform distribution than model-based MWF. In Fig. 8c, a zipper artifact in mGRE image is shown leading to abnormal overestimation of MWF in model-based MWF. The rPCA-MWF removed this to the S component r^2. For all cases, the rPCA-MWF shows a clearer image of the MWF. In the supplementary material (Fig. S3), images from other slices and comparison with magnitude model-based MWF for each of these cases are provided.

Results from a patient with demyelination (subject 10) is provided in Fig. 9. Image from the MT scan is also shown for comparison. The rPCA-MWF map shows decreased MWF at the genu of corpus callosum which is in agree with the MT scan (green arrow). The complex model-based MWF map, however, showed unclear representation.

VI. DISCUSSIONS

In this study, we proposed a data-driven source separation algorithm to map MWF from mGRE data as an alternative

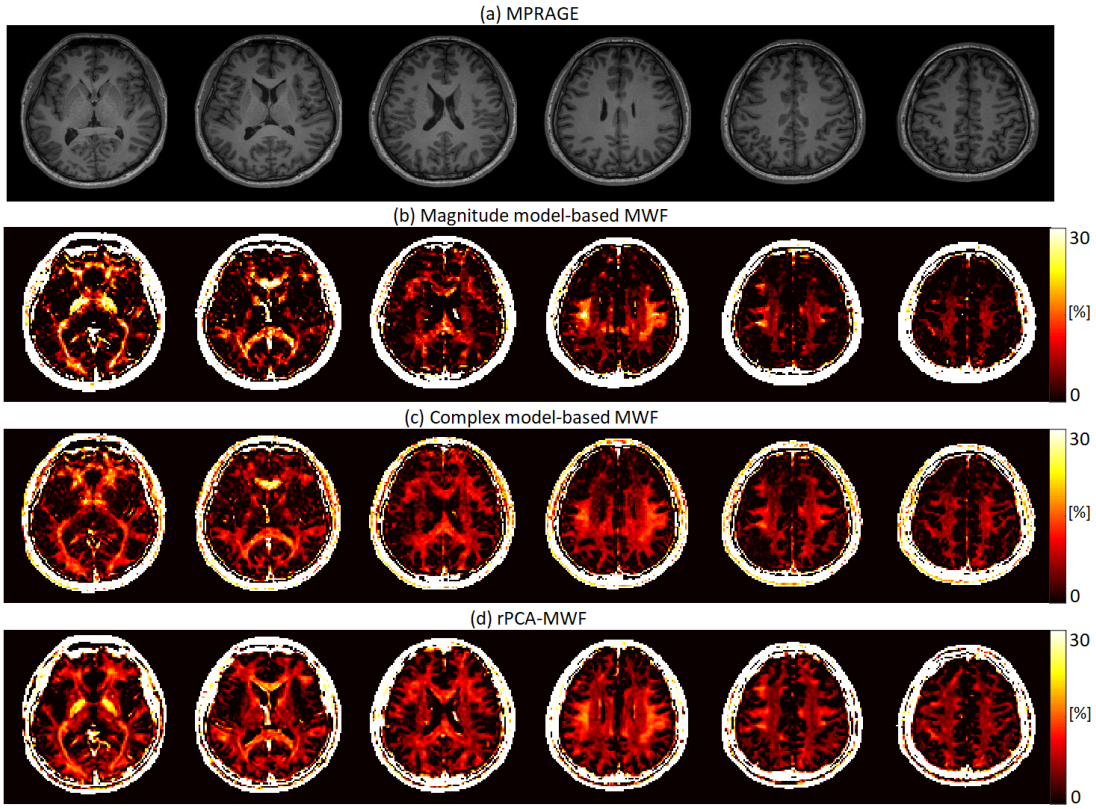

Fig. 6. Six representative slices from healthy volunteer (subject 1). (a) MPRAGE, (b) magnitude three pool model-based MWF, (c) complex three pool model-based MWF and (d) rPCA-MWF.

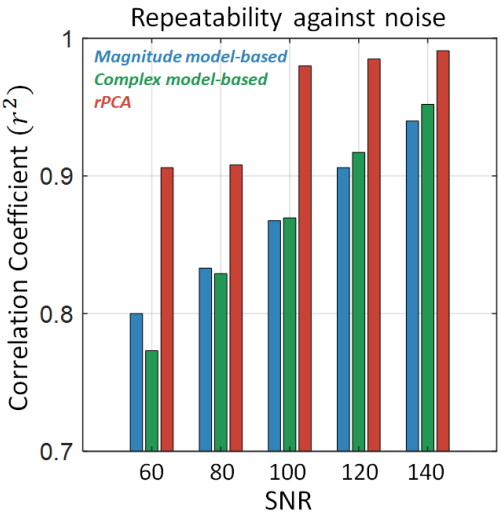

Fig. 7. The reproducibility of the MWF map as noise corruption. r^2 is Pearson's correlation coefficient between reference MWF map and noise additive MWF map.

to conventional MWF mapping methods. By optimizing the standard rPCA algorithm for MWF mapping, the separation of two unit-rank components and sparse component allowed robust MWF mapping as well as differentiating myelin water and axonal/extracellular water signals.

The incorporation of NMF and hankelization allowed preservation of the physical characteristics of tissue relaxation without a need for numerical modeling. First, NMF only allows additive combinations of signal sources by imposing non-negative constraint. This leads to the separated source signals to be represented in a more meaningful and interpretable feature [23]. Second, hankelization encourages exponential relaxation decays [28]–[43]. The enforcement of the unit-rankness of each mono-exponential decay promotes the differentiation of axonal/extracellular water and myelin water signal.

One of the major advantages of rPCA-MWF is artifact robustness. In conventional GRE-MWI, the procedure to solve model-based MWF is a nonlinear regression, fitting the parameters of the model that minimizes least squares residuals. The deviations in the signal derived from artifact misfit the fitting parameters of the model. In proposed rPCA-MWF, by model-free source separation, the deviated signal due to artifact representing non-exponential decay are decomposed to the $\mathbf{S}$ component. Consequently, the $\mathbf{L}_1$ and $\mathbf{L}_2$ components are free from out-of-model signal sources and supports the improvement of the reproducibility in rPCA-MWF. In particular, the S component was amplified with oscillatory signal for B0 inhomogeneity dominant voxel (Fig. S4). Although there was no numerical field inhomogeneity correction method implemented, the rPCA-MWF effectively separated non-exponentially decaying field inhomogeneity artifacts.

Another main advantage of rPCA-MWF is the noise robustness. In solving the objective function, the low rankness is enforced by singular value thresholding (SVT). The noisy subspace which yield small singular values are thresholded and the $\mathbf{L}_1$ and $\mathbf{L}_2$ components are represented by subspace with large singular values. Consequently, the rPCA-MWF mapped using the $\mathbf{L}_1$ and $\mathbf{L}_2$ components achieves noise robustness.

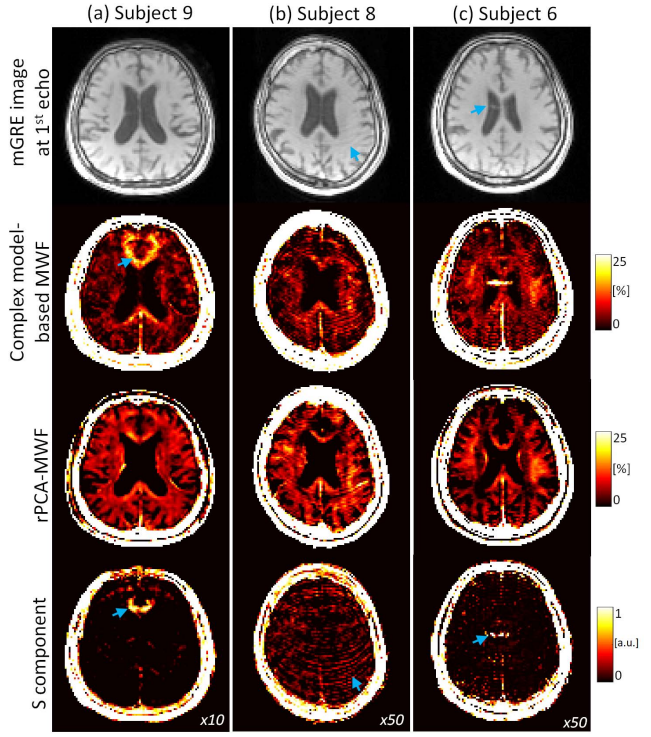

Fig. 8. Single representative slice when imaging artifacts are present. (a) B0 inhomogeneity (subject 9), (b) motion (subject 8) and (c) zipper (subject 6) artifacts. The rPCA-MWF shows reduced artefactual images. Note that the imaging artifacts depicted in mGRE images and complex model-based MWF are separated to the S component.

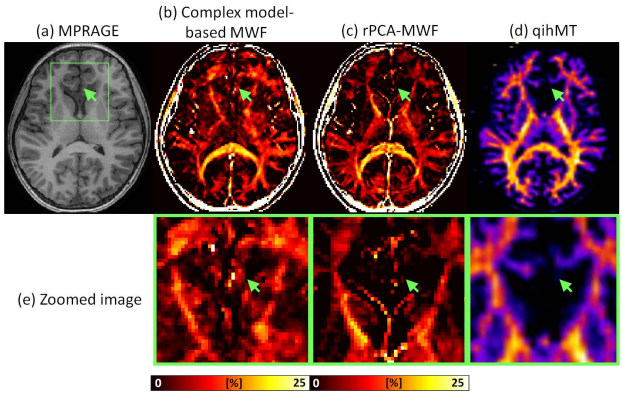

Fig. 9. Patient exam results for a single slice (subject 10). (a) T1 weighted image, (b) Complex model-based MWF, (c) rPCA-MWF (d) qihMT image and (e) the magnified image for demyelinated region. Note that the demyelination (green arrow at genu) is observed in rPCA-MWF, which is in agreement with the anatomic and qihMT image.

This supports the improvement of the reproducibility against noise in rPCA-MWF.

The amount of noise robustness of the $\mathbf{L}_1$ and $\mathbf{L}_2$ components is determined by the singular values of each component. As myelin water has lower signal than axonal/extracellular water, it is more susceptible to noise. Consequently, the robustness to noise was disrupted earlier for $\mathbf{L}_2$ (i.e., myelin water component) than $\mathbf{L}_1$ which results in mis-estimation of $\mathbf{L}_2$. The regularization parameters of rPCA-MWF were empirically determined to be robust for SNR $\sim$100 typical of in-vivo mGRE acquisition, however it could be further adjusted for lower SNR.

Another benefit of rPCA-MWF is the range of echo time. rPCA-MWF stabilized using 30 echoes with the last echo of 32 ms. Meanwhile, a typical regularized non-negative least squares MWF (i.e., rNNLS-MWF) requires more than 64 echoes (i.e., the last echo being longer than the slowly-decaying T_2^* component) [5]–[44]. Under the same hardware performances, TR of at least 80 ms is required to acquire 64 echoes. Consequently, the total scan time for rNNLS-MWF using 64 echoes is estimated to be 6 min 50 sec, which is 1.7 times longer than the scan time of this study. To avoid the increase of scan time and maintain a reasonable scan time for clinical application, we acquired 30 echoes. In addition, it has been reported that mGRE-MWF can robustly estimate MWF with this decreased number of [4], [21]. As rNNLS-MWF does not perform well under the given acquisition protocol due to lack of echo signals, it was not thoroughly compared in this study (Supplementary material Fig. S5 shows a demonstrative comparison of rNNLS-MWF and rPCA-MWF under the current acquisition protocol). In addition, a simulation study using numerical phantom shows that the RMSE for rPCA-MWF is lower than rNNLS-MWF, even assuming 64 echo acquisition (Supplementary material Fig. S6).

An additional benefit of the rPCA-MWF is the processing time. In our implementations, the complex model-based fitting and magnitude model-based fitting method required 69 secs and 31 secs per slice, respectively. The rPCA-MWF took 7.5 secs per slice and could cover whole 3D volume in under 5 mins.

Compared to multi-component model-based MWF, rPCA-MWF has two representative T_2^* for each voxel. The axonal water and extracellular water signals have T_2^* difference less than 20 ms at 7T, and therefore are difficult to differentiate [45]. In rPCA-MWF, these signals are represented as a single $\mathbf{L}_1$ component. Given a distribution of T_2^* values, the representative T_2^* of $\mathbf{L}_1$ and $\mathbf{L}_2$ corresponded to the logarithmic center of each distributed water pool (see simulation results in supplementary material Fig. S7) and to the literature T_2^* distribution in vivo (Fig. 5b). This supports that the separated $\mathbf{L}_1$ and $\mathbf{L}_2$ represent intra-/extracellular water and myelin water component respectively.

A potential limitation of the current rPCA-MWF is that only magnitude information has been used and each separated component is based on the magnitude signal. The susceptibility differences along fiber orientation of mGRE data perturbate the effective resonant frequencies of the water compartments [46]. While considering frequency offsets could improve the GRE-MWI [9]–[21], the lack of non-negativity and unit rankness of complex-valued signal made it difficult to implement a complex-value based rPCA-MWF. The absence of consideration for these orientational dependencies resulted in overestimation in iron rich regions (e.g., globus pallidus in deep gray matter of Fig. 6) [47], [48]. Extending rPCA-MWF to handle complex values in a different way is a future study.

REFERENCES

[1] A. Mackay, K. Whittall, J. Adler, D. Li, D. Paty, and D. Graeb, "*In vivo* visualization of myelin water in brain by magnetic resonance," *Magn. Reson. Med.*, vol. 31, no. 6, pp. 673–677, Jun. 1994.

[2] K. P. Whittall, A. L. Mackay, D. A. Graeb, R. A. Nugent, D. K. B. Li, and D. W. Paty, "*In vivo* measurement ofT2 distributions and water contents in normal human brain," *Magn. Reson. Med.*, vol. 37, no. 1, pp. 34–43, Jan. 1997.

[3] P. Van Gelderen, J. A. De Zwart, J. Lee, P. Sati, D. S. Reich, and J. H. Duyn, "Nonexponential T2* decay in white matter," *Magn. Reson. Med.*, vol. 67, no. 1, pp. 110–117, Jan. 2012.

[4] Y. Nam, J. Lee, D. Hwang, and D.-H. Kim, "Improved estimation of myelin water fraction using complex model fitting," *NeuroImage*, vol. 116, pp. 214–221, Aug. 2015.

[5] E. Alonso-Ortiz, I. R. Levesque, R. Paquin, and G. B. Pike, "Field inhomogeneity correction for gradient echo myelin water fraction imaging," *Magn. Reson. Med.*, vol. 78, no. 1, pp. 49–57, Jul. 2017.

[6] Y. P. Du *et al.*, "Fast multislice mapping of the myelin water fraction using multicompartment analysis of T decay at 3T: A preliminary postmortem study," *Magn. Reson. Med.*, vol. 58, no. 5, pp. 865–870, 2007.

[7] D. A. Yablonskiy, A. L. Sukstanskii, J. Luo, and X. Wang, "Voxel spread function method for correction of magnetic field inhomogeneity effects in quantitative gradient-echo-based MRI," *Magn. Reson. Med.*, vol. 70, no. 5, pp. 1283–1292, Nov. 2013.

[8] H. Lee, Y. Nam, H.-J. Lee, J.-J. Hsu, R. G. Henry, and D.-H. Kim, "Improved three-dimensional multi-echo gradient echo based myelin water fraction mapping with phase related artifact correction," *NeuroImage*, vol. 169, pp. 1–10, Apr. 2018.

[9] Y. Nam, D.-H. Kim, and J. Lee, "Physiological noise compensation in gradient-echo myelin water imaging," *NeuroImage*, vol. 120, pp. 345–349, Oct. 2015.

[10] K. J. Layton, M. Morelande, D. Wright, P. M. Farrell, B. Moran, and L. A. Johnston, "Modelling and estimation of multicomponent T_2 distributions," *IEEE Trans. Med. Imag.*, vol. 32, no. 8, pp. 1423–1434, Aug. 2013.

[11] M. Mckeown, "Independent component analysis of functional MRI: What is signal and what is noise?" *Current Opinion Neurobiol.*, vol. 13, no. 5, pp. 620–629, Oct. 2003.

[12] T. Nakai *et al.*, "Application of independent component analysis to magnetic resonance imaging for enhancing the contrast of gray and white matter," *NeuroImage*, vol. 21, no. 1, pp. 251–260, Jan. 2004.

[13] M. Molina-Romero *et al.*, "A diffusion model-free framework with echo time dependence for free-water elimination and brain tissue microstructure characterization," *Magn. Reson. Med.*, vol. 80, no. 5, pp. 2155–2172, 2018.

[14] R. Otazo, E. J. Candès, and D. K. Sodickson, "Low-rank plus sparse matrix decomposition for accelerated dynamic MRI with separation of background and dynamic components," *Magn. Reson. Med.*, vol. 73, no. 3, pp. 1125–1136, Mar. 2015.

[15] E. Levine, K. Stevens, C. Beaulieu, and B. Hargreaves, "Accelerated three-dimensional multispectral MRI with robust principal component analysis for separation of on- and off-resonance signals," *Magn. Reson. Med.*, vol. 79, no. 3, pp. 1495–1505, Mar. 2018.

[16] K. H. Jin, J.-Y. Um, D. Lee, J. Lee, S.-H. Park, and J. C. Ye, "MRI artifact correction using sparse + low-rank decomposition of annihilating filter-based Hankel matrix," *Magn. Reson. Med.*, vol. 78, no. 1, pp. 327–340, Jul. 2017.

[17] A. E. Campbell-Washburn *et al.*, "Using the robust principal component analysis algorithm to remove RF spike artifacts from MR images," *Magn. Reson. Med.*, vol. 75, no. 6, pp. 2517–2525, Jun. 2016.

[18] K. P. Whittall and A. L. Mackay, "Quantitative interpretation of NMR relaxation data," *J. Magn. Reson.*, vol. 84, no. 1, pp. 134–152, Aug. 1989.

[19] E. Alonso-Ortiz, I. R. Levesque, and G. B. Pike, "Multi-gradient-echo myelin water fraction imaging: Comparison to the multi-echo-spin-echo technique," *Magn. Reson. Med.*, vol. 79, no. 3, pp. 1439–1446, Mar. 2018.

[20] D. Hwang, D.-H. Kim, and Y. P. Du, "*In vivo* multi-slice mapping of myelin water content using T2* decay," *NeuroImage*, vol. 52, no. 1, pp. 198–204, Aug. 2010.

[21] H. Lee, Y. Nam, and D. Kim, "Echo time-range effects on gradient-echo based myelin water fraction mapping at 3T," *Magn. Reson. Med.*, vol. 81, no. 4, pp. 2799–2807, Apr. 2019.

[22] C. Ding, T. Li, and M. Jordan, "Convex and semi-nonnegative matrix factorizations," *IEEE Trans. Pattern Anal. Mach. Intell.*, vol. 32, no. 1, pp. 45–55, Jan. 2010.

[23] D. D. Lee and H. S. Seung, "Learning the parts of objects by non-negative matrix factorization," *Nature*, vol. 401, no. 6755, pp. 788–791, Oct. 1999.

[24] C. Boutsidis and E. Gallopoulos, "SVD based initialization: A head start for nonnegative matrix factorization," *Pattern Recognit.*, vol. 41, no. 4, pp. 1350–1362, Apr. 2008.

[25] Y. Xue, C. S. Tong, Y. Chen, and W.-S. Chen, "Clustering-based initialization for non-negative matrix factorization," *Appl. Math. Comput.*, vol. 205, no. 2, pp. 525–536, Nov. 2008.

[26] M. Rezaei and R. Boostani, "Using the genetic algorithm to enhance nonnegative matrix factorization initialization," *Expert Syst.*, vol. 31, no. 3, pp. 213–219, Jul. 2014.

[27] M. Fazel, T. K. Pong, D. Sun, and P. Tseng, "Hankel matrix rank minimization with applications to system identification and realization," *SIAM J. Matrix Anal. Appl.*, vol. 34, no. 3, pp. 946–977, Jan. 2013.

[28] P. Cao, X. Zhu, S. Tang, A. Leynes, A. Jakary, and P. E. Larson, "Shuffled magnetization-prepared multicontrast rapid gradient-echo imaging," *Magn. Reson. Med*, vol. 79, no. 1, pp. 62–70, Jan. 2018.

[29] J.-F. Cai, X. Qu, W. Xu, and G.-B. Ye, "Robust recovery of complex exponential signals from random Gaussian projections via low rank Hankel matrix reconstruction," *Appl. Comput. Harmon. Anal.*, vol. 41, no. 2, pp. 470–490, Sep. 2016.

[30] P. De Groen and B. De Moor, "The fit of a sum of exponentials to noisy data," *J. Comput. Appl. Math.*, vol. 20, pp. 175–187, Nov. 1987.

[31] E. J. Candès, X. Li, Y. Ma, and J. Wright, "Robust principal component analysis?" *J. ACM*, vol. 58, no. 3, Jun. 2011.

[32] J. D. Trzasko, "Exploiting local low-rank structure in higher-dimensional MRI applications," *Proc. SPIE*, vol. 8858, Sep. 2013, Art. no. 885821.

[33] T. Zhang, J. M. Pauly, and I. R. Levesque, "Accelerating parameter mapping with a locally low rank constraint," *Magn. Reson. Med.*, vol. 73, no. 2, pp. 655–661, Feb. 2015.

[34] G. L. da Cruz, A. Bustin, O. Jaubert, T. Schneider, R. M. Botnar, and C. Prieto, "Sparsity and locally low rank regularization for MR fingerprinting," *Magn. Reson. Med.*, vol. 81, no. 6, pp. 3530–3543, 2019.

[35] Y. Wang, J. Yang, W. Yin, and Y. Zhang, "A new alternating minimization algorithm for total variation image reconstruction," *SIAM J. Imag. Sci.*, vol. 1, no. 3, pp. 248–272, Jan. 2008.

[36] T. Goldstein and S. Osher, "The split Bregman method for L_1-regularized problems," *SIAM J. Imag. Sci.*, vol. 2, no. 2, pp. 323–343, Jan. 2009.

[37] S. Boyd, "Distributed optimization and statistical learning via the alternating direction method of multipliers," *Found. Trends Mach. Learn.*, vol. 3, no. 1, pp. 1–122, 2010.

[38] J.-F. Cai, E. J. Candès, and Z. Shen, "A singular value thresholding algorithm for matrix completion," *SIAM J. Optim.*, vol. 20, no. 4, pp. 1956–1982, Jan. 2010.

[39] R. M. Kroeker and R. M. Henkelman, "Analysis of biological NMR relaxation data with continuous distributions of relaxation times," *J. Magn. Reson.*, vol. 69, no. 2, pp. 218–235, Sep. 1986.

[40] S. J. Graham, P. L. Stanchev, and M. J. Bronskill, "Criteria for analysis of multicomponent tissue T2 relaxation data," *Magn. Reson. Med.*, vol. 35, no. 3, pp. 370–378, Mar. 1996.

[41] B. L. Geeraert *et al.*, "A comparison of inhomogeneous magnetization transfer, myelin volume fraction, and diffusion tensor imaging measures in healthy children," *NeuroImage*, vol. 182, pp. 343–350, Nov. 2018.

[42] S. M. Smith, "Fast robust automated brain extraction," *Hum. Brain Mapping*, vol. 17, no. 3, pp. 143–155, Nov. 2002.

[43] M. Zimmermann, Z. Abbas, K. Dzieciol, and N. J. Shah, "Accelerated parameter mapping of multiple-echo gradient-echo data using model-based iterative reconstruction," *IEEE Trans. Med. Imag.*, vol. 37, no. 2, pp. 626–637, Feb. 2018.

[44] C. Lenz, M. Klarhöfer, and K. Scheffler, "Feasibility of *in vivo* myelin water imaging using 3D multigradient-echo pulse sequences," *Magn. Reson. Med.*, vol. 68, no. 2, pp. 523–528, Aug. 2012.

[45] P. Sati *et al.*, "Micro-compartment specific T2* relaxation in the brain," *NeuroImage*, vol. 77, pp. 268–278, Aug. 2013.

[46] S. Wharton and R. Bowtell, "Fiber orientation-dependent white matter contrast in gradient echo MRI," *Proc. Nat. Acad. Sci. USA*, vol. 109, no. 45, pp. 18559–18564, Nov. 2012.

[47] C. Langkammer *et al.*, "Quantitative susceptibility mapping (QSM) as a means to measure brain iron? A post mortem validation study," *NeuroImage*, vol. 62, no. 3, pp. 1593–1599, Sep. 2012.

[48] B. Yao, T. Li, P. Gelderen, K. Shmueli, J. Dezwart, and J. Duyn, "Susceptibility contrast in high field MRI of human brain as a function of tissue iron content," *NeuroImage*, vol. 44, no. 4, pp. 1259–1266, Feb. 2009.